ELSEVIER

Contents lists available at ScienceDirect

# Chemical Engineering Journal

journal homepage: www.elsevier.com/locate/cej





# Bimetallic copper-bismuth microtubular electrodes with tunable interfaces for efficient electrochemical reduction of CO<sub>2</sub> to formate

Beibei Ma <sup>a,b</sup>, Hesamoddin Rabiee <sup>c,\*</sup>, Guoliang Chen <sup>d</sup>, Yizhu Kuang <sup>d</sup>, Tianjiu Zhu <sup>a</sup>, Penghui Yan <sup>a</sup>, Lei Ge <sup>b,d,\*\*</sup>, Zhonghua Zhu <sup>a,b,\*\*</sup>

- <sup>a</sup> School of Chemical Engineering, The University of Queensland, Brisbane, QLD, 4072, Australia
- <sup>b</sup> ARC Centre of Excellence for Green Electrochemical Transformation of Carbon Dioxide, Brisbane, QLD, 4072, Australia
- <sup>c</sup> Department of Chemistry, Biochemistry and Pharmaceutical Sciences, University of Bern, Freiestrasse 3, Bern, 3012, Switzerland
- d Centre for Future Materials, School of Engineering, University of Southern Queensland, Springfield, QLD, 4300, Australia

#### ARTICLEINFO

#### Keywords:

Bimetallic microtubular gas-diffusion electrode Cu/Bi interface Electrochemical reduction of CO<sub>2</sub> Formate production

#### ABSTRACT

Electrochemical reduction of CO<sub>2</sub> (CO<sub>2</sub>RR) offers a sustainable route for CO<sub>2</sub> utilization, with emerging carbonfree gas-diffusion electrodes (GDEs) mitigating the flooding issues that limit its performance. Metal-based microtubular (hollow fiber) GDEs (HFGDEs) are particularly promising due to enhanced mass transfer by gas flow-through feed, superior charge transfer and mechanical strength. Copper-based GDEs are efficient for CO<sub>2</sub>RR but often lack selectivity. Introducing bimetallic interfaces on GDE surfaces is an effective strategy to modulate CO<sub>2</sub>RR pathways. Herein, CuBi bimetallic HFGDEs were fabricated for CO<sub>2</sub>RR through a facile premixing approach. The CuBi HFGDE with 10 wt% Bi incorporation (CuBi-10) created abundant Cu/Bi interfaces at the triple-phase boundaries, while preserving the CO2 accessibility of the HFGDEs. Operating CuBi HFGDE in flowthrough GDE mode ensured sufficient CO2 supply, effectively suppressing HER and enhancing formate selectivity. CuBi-10 achieved over 90 % Faradaic efficiency (FE) for formate across a low potential window (-0.9 to  $-1.1~\mathrm{V}$  vs. RHE), significantly outperforming monometallic Cu HFGDE (formate FE <20~% at all applied potentials). The superior formate partial current density of CuBi-10 over Cu HFGDE (more than 5 times higher at -1.1 V vs. RHE) was due to the increased active sites and lower charge transfer resistance. In-situ Raman analysis revealed that the Cu/Bi interface effectively suppresses HER and promotes the \*OCHO pathway during CO2-toformate conversion. This work presents the promise toward designing metal-based HFGDEs with bimetallic interfaces at triple-phase boundaries for selective CO2RR to formate.

# 1. Introduction

Electrochemical  $CO_2$  reduction reaction  $(CO_2RR)$  has rapidly emerged as a promising technique to address rising  $CO_2$  emissions by selectively converting  $CO_2$  into value-added products  $(C_1$  and  $C_{2+}$  products) at ambient conditions, while also storing the intermittent electric energy in high-energy-density fuels [1–4]. Single-carbon  $(C_1)$  formate (formic acid) is considered a key target product in  $CO_2RR$  as it shows the highest value generated per mole of electrons [5]. It can serve as liquid fuel for fuel cells, stable and safe hydrogen carrier, and versatile building block in the synthesis of chemicals and pharmaceuticals [6–9]. Although substantial progress has been made in achieving high selectivity toward the desired product and overcoming the sluggish kinetics

of  $CO_2RR$ , further improvements still rely on the rational design of both electrode and electrocatalysts [10–13].

Gas-diffusion electrodes (GDEs) play a critical role in enhancing CO<sub>2</sub>RR performance. By enabling a continuous gaseous reactant supply and reducing the CO<sub>2</sub> diffusion pathway compared to the planar configuration, GDEs improve CO<sub>2</sub> accessibility to catalytic sites [14], thus boosting overall reaction efficiency [15]. However, common planar GDEs, which incorporate a carbon-based gas diffusion layer, suffer from electrowetting and electrolyte penetration, resulting in undesired hydrogen evolution reaction (HER) and salt precipitation, thereby impairing the CO<sub>2</sub>RR performance [16]. To overcome these limitations, carbon-free GDEs, polymer-based GDEs [17–19] and metal-based GDEs [20,21], have been developed, in which metal-based GDEs possess the

<sup>\*</sup> Correspondence to: H. Rabiee, Department of Chemistry, Biochemistry and Pharmaceutical Sciences, University of Bern, Freiestrasse 3, Bern, 3012, Switzerland.

<sup>\*\*</sup> Corresponding authors at: ARC Centre of Excellence for Green Electrochemical Transformation of Carbon Dioxide, Brisbane, QLD, 4072, Australia. E-mail addresses: hesamoddin.rabiee@unibe.ch (H. Rabiee), lei.ge@unisq.edu.au (L. Ge), z.zhu@uq.edu.au (Z. Zhu).

inherent superiority of easier current collection [22].

Metal-based hollow fiber GDEs (HFGDEs) represent a promising opportunity to combine the advancements in metal-based GDE and microtubular design [23]. Its self-supported all-metal skeleton offers easy current collection, strong mechanical strength and allows for in-situ surface modification (such as electrodeposition [24-27], alloying [9] and doping [28]). Moreover, HFGDEs do not need the additional gas chamber that feeds gaseous reactant, instead, CO2 in the inner tube of HFGDE can build up pressure and then be purged through the pores on the tubular wall and be delivered to catalytic sites on the outer surface, adopting a flow-through mode [29,30]. This mode reduces the gas concentration gradient compared to the flow-by mode, resulting in an enhanced local CO2 concentration and less HER on the catalytically active surface [31,32], facilitating the achievement of industrial-level current densities by Cu-, Ag- and Bi-based HFGDEs [33-35]. Besides, the scalable fabrication and the small radial dimensions of HFGDEs underscore their potential for large-scale application [36].

In addition to electrode architecture, catalyst composition, particularly through the engineering of bimetallic interfaces, is key to tuning reaction pathways and determining CO<sub>2</sub>RR selectivity. Cu-based catalysts have shown outstanding efficiency in reducing CO2 into a wide variety of hydrocarbons and oxygenates (sixteen distinct C<sub>1</sub>-C<sub>3</sub> products can be detected) [37,38]. However, it accompanies poor selectivity toward desired products [39]. An effective strategy is to construct a bimetallic system to break the scaling relation on Cu surface, where Cu and another metal (e.g. Ag, Au, Pd, Sn or Bi) can function synergistically via engineering lattice strain, tuning electron density, asymmetric/tandem catalytic sites and forming unique morphologies, leading to enhanced electrocatalytic performance [40-45]. Bi stands out for its low toxicity and electrochemical behavior of converting CO2 to formate in the CO2RR process due to its flexible and versatile coordination structure and low HER activity [46-48]. The formation of CuBi nanoparticles was proposed to alter the CO<sub>2</sub>RR pathway via tuning the Cu:Bi atomic fraction, specifically, lower Bi content (9.1 %) favours CO2-to-CO conversion, whereas an increased Bi ratio (19.2 %) promotes CO2-toformate pathway [49]. Notably, MOF-derived CuBi bimetallic catalysts could form new phase (such as Bi<sub>2</sub>CuO<sub>4</sub>) or generate electron-rich Bi, thus enhancing CO2 chemisorption and stabilizing intermediate (\*COOH and HCOO\*) to achieve high selectivity over formate up to 95 % [50,51].

In this study, we design high-performance HFGDEs with abundant Cu/Bi bimetallic interfaces at the triple-phase boundary during CO<sub>2</sub>RR by utilizing metal-based HFGDE architecture. A facile strategy was developed to uniformly distribute the Bi phase within the Cu phase via premixing the Bi and Cu particles in precursor solutions. A composition with 10 wt% Bi achieved an ideal balance between Cu/Bi interface distribution at the pore edges and the accessible pore area on the electrode surface. This resulted in improved CO<sub>2</sub>RR performance regarding Faradaic efficiencies of formate and electrocatalytic activity compared to monometallic Cu HFGDE. Operating the CuBi HFGDE in flow-through GDE mode effectively suppressed HER and enhanced charge transfer and CO<sub>2</sub> supply at triple-phase boundaries, achieving FE > 90 % for formate formation. Moreover, in-situ Raman spectroscopy revealed that the Cu/ Bi interface suppresses HER and promotes \*OCHO pathway during CO2to-formate conversion. This research exhibited a rational design strategy for bimetallic-based gas-diffusion electrodes by engineering bimetallic interfaces at triple-phase boundaries, enabling enhanced formate production.

# 2. Experimental method

# 2.1. Chemicals

Copper powder (particle size of 8  $\mu$ m, 99.5 % purity) was purchased from US Research Nanomaterials. Bismuth powder (particle size <25  $\mu$ m, 99.0 + % purity) was purchased from SkySpring Nanomaterials.

Polyethersulfone particles (PES Ultra son) were from BASF, Germany. *N*-methyl-2-pyrronlidone (NMP) and potassium bicarbonate ( $\geq$ 99.5 %) were purchased from Sigma. Fluorescein sodium salt was purchased from ChemSupply, Australia. Ultrapure water used in all the experiments was acquired from Arium® Pro UF Ultrapure Water System (Sartorius, 18.2 M $\Omega$ ·cm).

#### 2.2. CuBi bimetallic hollow fiber GDE fabrication

The CuBi hollow fiber gas-diffusion electrodes (HFGDEs) were fabricated through a dry-wet (phase inversion) spinning procedure and calcining process (as shown in Fig. S1). Firstly, the precursor solution of metal powders, binder (PES) and solvent (NMP) was mixed by ball mill machine for 48 h, with the respective ratio of 70 wt%:7.5 wt%:22.5 wt %. A series of CuBi precursor solutions were prepared with the different copper and bismuth weight ratios, which were 0 wt%, 5 wt%, 10 wt%, 20 wt% and 30 wt% of bismuth powders in the mixed metal powders. After the polymer and metal powder solutions were well mixed, they were vacuumed for 2 h to remove air bubbles. Next, the precursor solution was poured into a stainless-steel vessel and then extruded through a spinneret rig into a tap water bath, while deionized water was continuously purged through the bore of the spinneret (with a flow rate of 25 mL min-1) during the extrusion. The green hollow fibers were left in water for 24 h to remove NMP. Subsequently, the obtained green hollow fibers were calcinated in air atmosphere in a tube furnace at 600  $^{\circ}$ C for 3 h to burn out the polymer (PES) and then reduced at 500  $^{\circ}$ C in the H<sub>2</sub> atmosphere for 3 h and aged at 700 °C in argon for another 3 h (heating/cooling rate was 5 °C/min for all procedures performed in the furnace). All samples were kept in an N<sub>2</sub> atmosphere until further tests.

#### 2.3. Material characterization

The surface morphology and cross-section of the as-prepared HFGDEs were investigated by field emission scanning electron microscopy (FESEM, JOEL-7100 F), and the distribution of copper and bismuth was visualized by the backscattered electron (BSE) image. Energy dispersive X-ray spectroscopy (EDS) was used for element mapping. The separated Cu and Bi phases on the Cu/Bi interface were analyzed by high-resolution transmission electron microscopy (HRTEM, Hitachi HF5000, Japan). The bimetallic crystal structure of the HFGDEs was analyzed by X-ray diffraction (XRD, Bruker SmartLab, Cu K $\alpha$  ( $\lambda$  = 1.5405 Å) radiation source, Japan). The compositions and valence state of the HFGDEs were examined by X-ray photoelectron spectroscopy (XPS, Kratos Axis ULTRA XPS with a monochromatic Al Kα radiation source (1486.6 eV) at 15 kV (10 mA) and a 165 mm hemispherical electron energy analyzer). All XPS data were processed by CASA® software, with the calibration of the C1s signal to 284.8 eV as the reference. The pore distribution of the HFGDEs was visualized by confocal microscope (ZEISS LSM 900 Upright Laser Scanning Confocal Microscope, with the objective of  $10 \times /0.45$  Dry DIC M27 and a 488 nm diode for laser line). To prepare the samples for confocal imaging, one end of the HFGDEs was blocked by epoxy, the dye solution (10 mM of fluorescein sodium salt solution) was injected into the hollow fiber via the other end and then purged out through the pores on the tubular wall with airflow at a flow rate of 500 mL min<sup>-1</sup>. An ultrasonic water bath was applied for 5 min as the next step to remove the dye from the outer surface of the HFGDEs. This way, the dye trace inside the pores was reserved for confocal imaging. The calculations of pore area percentage and the proportion of pores with Cu/Bi interface were conducted using ImageJ and Adobe Photoshop to analysis surface SEM images. Calculation of CO2 permeability and computational fluid dynamic (CFD) calculations are provided in Supplementary Information.

### 2.4. CO<sub>2</sub> electrochemical reduction and analysis of products

All the electrochemical measurements were carried out using a

Biologic SP-200 potentiostat under ambient pressure and temperature. The electrochemical reduction of  $\rm CO_2$  was conducted in a three-electrode H-cell (Fig. S2a). The working electrode was the as-prepared hollow fiber GDEs and the counter electrode was Pt foil (1 cm  $\times$  1 cm). The reference electrode was an Ag/AgCl (3 M NaCl, BASi, USA), which was placed in a Luggin probe (filled with 3 M NaCl) to be close to the working electrode. The cathode (HFGDE) length was 2.0–2.5 cm for all the tests. Nafion 117 membrane (from the Fuel Cell store) was used as a proton exchange membrane between the cathode and anode chambers. The long-term stability test was conducted using a customized-flow cell (Fig. S2b), with HFGDEs as the working electrode, a Pt wire as the counter electrode, and an Ag/AgCl (filled with 3.5 M KCl) as reference electrode. The catholyte and anolyte used for all electrochemical tests were 0.5 M KHCO<sub>3</sub> unless otherwise stated.

Before any electrochemical measurements, the catholyte was saturated with  $CO_2$  to reach pH equilibrium state.  $CO_2$  was continuously purged into the catholyte through the pores on the hollow fiber wall (one end of the HFGDE was sealed with epoxy, while the other end was the entrance of  $CO_2$ ) for 30 min. Catholyte was under magnetic stirring throughout the measurements to refresh electrolyte/product concentrations near the HFGDEs and facilitate the transfer of  $CO_2$ . All the electrochemical tests were performed while purging  $CO_2$  into catholyte, the flow rate of  $CO_2$  was 30 mL min-1 and controlled by a mass flow controller (Bronkhorst,  $\pm 1$  % resolution, Netherlands).

The reduction CV scanned from -1~V to -1.6~V vs. Ag/AgCl was applied to condition the HFGDEs. The current densities (mA cm- $^2$ ) in the main text and supplementary materials were normalized to the outer surface area of tubular electrodes. The potentials to the reversible hydrogen electrode (RHE) were converted using the following equation:  $E~(V~vs.~RHE) = E~(V~vs.~Ag/AgCl) + E_{Ag/AgCl}^0 + 0.0591pH.$ 

where  $E_{Ag/AgCl}^{O}$  is 0.209 V for the Ag/AgCl reference electrode filled with 3 M NaCl, the catholyte pH (Table S1) was measured by a pH meter probe (LAQUAtwin-pH-33, HORIBA).

The linear scanning voltammograms (LSVs) of HFGDEs were scanned in the potential range from  $-0.4\ V$  to  $-1.4\ V$  vs. RHE with a sweeping rate of 5 mV/s. Electrochemical impedance spectroscopy (EIS) tests were conducted at  $-1.0\ V$  (vs. RHE) from 100 kHz to 0.1 Hz for all HFGDEs. The electric double-layer capacitance (Cdl) of the CuBi HFGDEs was evaluated via the CV plots obtained at different scan rates from 20 to 100 mV/s (20 mV/s intervals) over a 0.1 V electrochemical window. The following equation was used to calculate Cdls:

$$Cdl = J \bigg/ \bigg( \frac{dV}{dt} \bigg)$$

Cdl is the capacitance, J is the current density in the center of 0.1 V electrochemical window and  $\frac{dV}{dt}$  is the CV scan rates.

Chronoamperometry was conducted for 1 h at various potentials from -0.7~V to -1.2~V vs. RHE with intervals of 0.1 V, to determine the faradaic efficiency (FE) of products. Liquid and gaseous products sampling started 30 min after each potential applied, to ensure that the cell reached the steady state. The liquid sample was measured by high-performance liquid chromatography (HPLC, Shimadzu Corporation, Japan), equipped with a UV–vis detector (SPD-20 A/20AV) and a Hi-Plex column (7.7  $\times$  300 mm, 8  $\mu m$ , Agilent Technologies, Inc.). The faradaic efficiency of formate was calculated by the following equation:

$$FE_{formate} = \frac{e_i \times F \times nformate}{O}$$

Here,  $e_i$  is the electron transfer number to produce one mole of products (e is 2 for formate), F is Faraday's constant (96,458C mol-1),  $n_{formate}$  is the mole of generated formate (by HPLC) and Q is the total charge during the  $CO_2RR$ .

Gaseous products were monitored by gas chromatography (GC, Shimadzu 2014). Carbon products were detected by a flame ionization detector (FID), while H<sub>2</sub> was detected by a thermal conductivity detector

(TCD). The following equation was used to calculate the faradaic efficiency of gaseous products:

$$FEi = \frac{e_i \times F \times P \times \nu \times x_i}{I \times R \times T} \times 100$$

where  $e_i$  is 2 for  $H_2$  and CO, P is the atmospheric pressure (101,300 Pa),  $\nu$  is the outlet gas flow rate,  $x_i$  is the concentration of gaseous products (by GC), J is the current during gaseous product sampling, R is gas constant (8.314 J mol<sup>-1</sup> k<sup>-1</sup>) and T is the ambient temperature (298 K).

#### 2.5. In-situ Raman spectroscopy

In-situ Raman measurements were conducted in a customized electrochemical cell and a Raman spectrometer (Renishaw) under fixed potentials in  $\rm CO_2$ -saturated 0.5 M KHCO $_3$  electrolyte, in which the 3.5 M KCl-saturated Ag/AgCl and Pt plate were used as the reference and counter electrode, respectively. HFGDEs (Cu HF, CuBi-10, CuBi-20) were used at the working electrodes in the electrolysis cell. A waterimmersed objective was selected as the Raman lens. The Raman shift was calibrated to 520 cm $^{-1}$  using a Si source. Before each experiment, the electrolysis cell with 0.5 M KHCO $_3$  was bubbled with 20 mL/min  $\rm CO_2$  for 20 min. A 10 mL/min  $\rm CO_2$  flow was kept during Raman analysis. The Raman spectra were continuously recorded without time intervals, and in the meantime, the potential was fixed at a range of  $\rm -0.2$  to  $\rm -0.8$  V (vs. RHE). Each Raman curve was obtained using a commercially available data-processing program (Wire 5.6 software).

#### 3. Results and discussion

#### 3.1. Microstructure characterizations

The triple-phase interface is where the catalyst surface, CO2, and the aqueous electrolyte converge, and plays a critical role in CO2RR by impacting active sites accessibility and the electron/mass transfer [52]. As illustrated in Fig. 1a, the metal-based HFGDE design enables the facile formation of Cu/Bi bimetallic interfaces at the triple-phase boundary by simply premixing Cu and Bi particles in the precursors, which leads to a uniform distribution of the Bi phase within the Cu matrix throughout the HFGDE skeleton. The prepared CuBi HFGDEs were denoted as CuBi-x, where x represents the weight ratio of Bi in the metal mixture. After the addition of Bi, CuBi HFGDEs exhibited an increased surface luster compared to the Cu HFGDE and showed a grey color on the surface of CuBi-20 and CuBi-30 (Fig. 1b). The cross-section SEM images (Figs. 1c, S3a3-e3, a4-e4) demonstrated the uniform wall thickness of 130-170 µm was obtained. As shown in Figs. 1e1, f1 and S3a1-e1, all the hollow fibers showed relatively smooth surface morphology on the outer layer regardless of the addition of Bi. For Cu HFGDE (Figs. 1e1, S3a1), sintered Cu particles aggregated and formed a highly uniform porous structure over the tubular wall, which promotes the delivery of CO<sub>2</sub> to the catalyst/electrolyte interface to generate a triple-phase region for efficient CO2RR [29]. After the addition of Bi (Figs. 1f1, S3b1-e1), partial space between Cu particles was filled with a less smooth texture, which was the melted Bi under the reduction temperature of 500 °C (the melting point of Bi is 271.4 °C). Backscattered electron images (BSE) (Figs. 1e2, f2, S3a2-e2) were employed to distinguish Cu and Bi more clearly, and Bi was homogeneously distributed between Cu, indicating the co-existence of Cu and Bi phases uniformly. This was confirmed by the EDS spectrum (Fig. S4) that the smooth part (dark grey area in BES images) was copper, and the relatively rough surface (light grey area in BES images) was bismuth. The Bi mass ratios of CuBi HFGDEs from the quantification of EDS (Table S2) were close to the initial addition ratio of Bi, indicating uniform distribution of Cu and Bi. Further validation of the distribution of Cu and Bi was performed by EDS analysis on CuBi-10 (Fig. 1g), which showed Cu/ Bi interfaces on the surface of CuBi HFGDE. As can be observed from

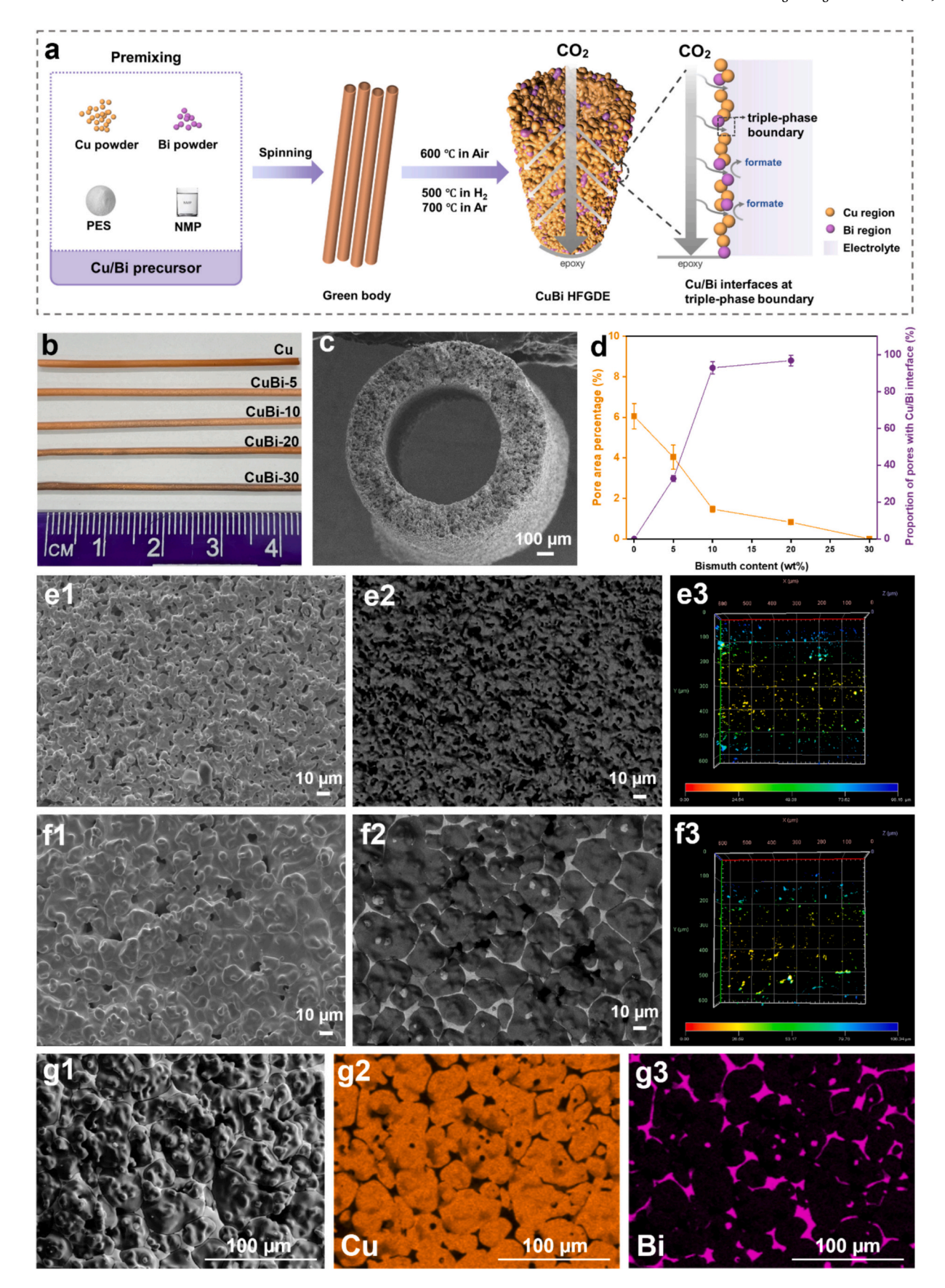


Fig. 1. a) Schematic of the formation of Cu/Bi interface at the triple-phase boundary; b) optical photo images of Cu and CuBi HFGDE; c) cross-section SEM images of CuBi-10; d) pore area percentage trend and the proportion of pores with Cu/Bi interface of CuBi HFGDEs with different Bi weight ratio; surface SEM, backscattered electron and confocal microscopy images of e1, e2, e3) Cu HFGDE and f1, f2, f3) CuBi-10; SEM-EDS analysis area g1), element mapping of g2) Cu and g3) Bi.

SEM images, the porosity of CuBi HFGDEs deteriorated gradually with the increasing amount of Bi. CuBi-5 (Fig. S3b1, b2) showed a similar morphology to Cu HFGDE (Fig. S3a1, a2) as the small amount of Bi had a minor impact on the porosity of the HFGDEs. CuBi-10 (Fig. S3c1, c2) had fewer pores when compared with CuBi-5, yet there were abundant Cu/Bi interfaces on the edge of the pores, which allowed Cu and Bi to perform a synergistic effect in the triple-phase region during CO<sub>2</sub>RR. When the Bi content increased to 20 wt% (Fig. S3d1, d2), a significant portion of pores became obstructed by the molten Bi. With a further increase to 30 wt% Bi (Fig. S3e1, e2), the pores were entirely occluded, thereby inhibiting the ability to facilitate CO<sub>2</sub>RR under GDE mode. The pressure drops across the HFGDEs gradually increased with rising Bi mass ratio, indicating partial pore blockage caused by increased Bi content (Table S3). To further investigate changes in porosity, confocal microscopy was conducted to visualize the pore distribution of the HFGDEs (Figs. 1e3, f3, S5). The fluorescent regions indicate retained dye within the pores of the tubular wall, showing that the porosity decreased with the increase of Bi weight ratio in CuBi HFGDEs. Despite this reduction, CuBi-5, CuBi-10 and CuBi-20 exhibit sufficient gas permeability at the CO<sub>2</sub> flow rate of 30 mL min<sup>-1</sup>, all exceeding the 2000 GPU threshold, affirming their fast gas transport capacity [53]. To elucidate the relationship between pore area and Cu/Bi interface, the downtrend of pore area percentage with increasing Bi weight ratio, along with the proportion of pores containing Cu/Bi interfaces of as-prepared CuBi HFGDEs were illustrated in Fig. 1d. Though CuBi-20 possessed Cu/Bi interfaces at almost every pore edge, the overall pore area percentage was much lower than CuBi-5 and CuBi-10, leading to much less triple-phase interface regions. CuBi-10, with the optimal content of Bi and microstructure, enables the most effective participation of Cu/Bi interfaces during CO<sub>2</sub>RR.

The surface crystalline structures of as-prepared HFGDEs were investigated by X-ray diffraction (XRD). As shown in Fig. 2a,

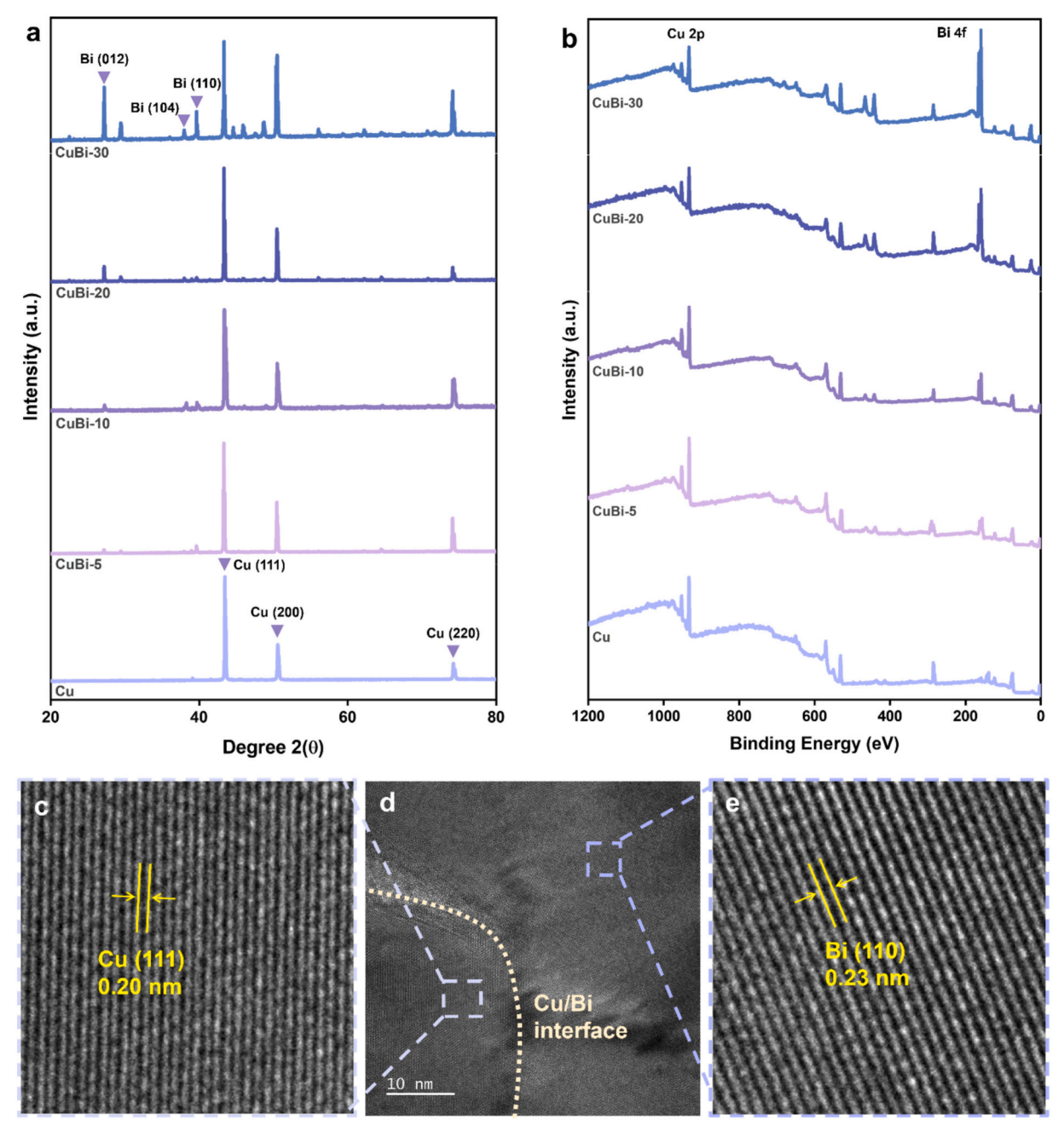


Fig. 2. a) XRD patterns and b) XPS spectra of HFGDEs; High-resolution TEM images of c) Cu phase, d) Cu/Bi interface and e) Bi phase.

characteristic peaks of Cu, which are attributed to Cu (111), Cu (200) and Cu (222) planes, can be observed in all the patterns. On the surface of CuBi HFGDEs, new peaks regarding Bi (012), Bi (104) and Bi (110) planes were observed, yet these peaks were weaker than the Cu peaks as the weight ratio of Bi was much lower than Cu (Bi was with the content ratio of 5 wt%, 10 wt%, 20 wt% and 30 wt%, respectively). The relative intensity of Bi peaks, especially Bi (012), increased with the rising ratio of Bi. It confirmed that the Bi phase was successfully distributed between Cu HFGDEs, which aligned with the results from SEM images.

The XPS surveys of Cu hollow fibers and CuBi hollow fibers demonstrated the surface compositions and oxidation state of copper and bismuth (Fig. 2b). The primary peaks of Cu 2p at 932.6 eV and 952.4 eV were found in all the HFGDEs, which were attributed to Cu  $2p_{3/2}$  and Cu  $2p_{1/2}$ , respectively. Compared with Cu HFGDEs, CuBi HFGDEs showed the characteristic peaks of Bi 4f at 159 eV and 164 eV, regarding Bi<sup>3+</sup>  $4f_{7/2}$  and Bi<sup>3+</sup>  $4f_{5/2}$ , respectively. The appearance of Bi 4f signals indicated the existence of Bi on the surface of CuBi hollow fibers. Though the hollow fibers were reduced by H<sub>2</sub>, the existence of Bi<sup>3+</sup> is unavoidable due to the oxidation occurring in air [54].

To further investigate the Cu/Bi interface, the crystal structure at the surface of CuBi HFGDE was examined using high-resolution TEM (Figs. 2c, d, e and S6). Distinct plane boundaries between Cu and Bi were clearly observed, consistent with the results from SEM. In the Cu phase (Fig. 2c), lattice fringes with a d-spacing of 0.20 nm, corresponding to Cu (111) planes, were evident. In the Bi phase (Fig. 2e), lattice stripes with a d-spacing of 0.23 nm that are attributed to Bi (110) plane were observed. These observations not only align with the XRD results but also provide direct confirmation of the formation of the Cu/Bi interface.

# 3.2. ${\it CO}_2$ delivery in HFGDE configuration under non-GDE mode and GDE mode

One superiority of the HFGDE is that it can adopt the flow-through GDE mode, which effectively minimizes the gas concentration gradient relative to the flow-by mode, resulting in enhanced local CO2 concentration and less HER [36]. To elucidate the CO2 delivery mechanism enabled by HFGDE design, we evaluated the CO<sub>2</sub>RR performance of CuBi-10 under both non-GDE and GDE modes. In the non-GDE mode (Fig. 3a), gaseous CO2 first dissolves in the bulk electrolyte and subsequently diffuses toward the electrode surface via a long-diffusion path, leading to elevated mass transport resistance and insufficient CO2 supply. In contrast, the GDE mode (Fig. 3b) facilitates continuous  $CO_2$  delivery from the lumen side of the hollow fiber electrode, allowing it to permeate through the porous tubular wall and directly reach the active sites, thereby ensuring sufficient CO2 availability at triple-phase interfaces. GDE mode significantly improved the formate selectivity (Fig. 3c). FE of formate in GDE mode was much higher than that in non-GDE mode at all applied potentials, and HER was effectively suppressed. The CO2RR activity in GDE mode demonstrated enhancement in the formate partial current density (115 mA cm $^{-2}$  at -1.3 V vs. RHE), which is more than twice observed in non-GDE mode (55 mA cm<sup>-2</sup> at -1.3 V vs. RHE) (Fig. 3d). Electrochemical impedance spectroscopy (EIS) tests at -1.0 V vs. RHE (Fig. 3d, inserted figure) further confirmed the improved kinetics in GDE mode, showing a much lower charge transfer resistance (2.5  $\Omega$  cm<sup>-2</sup>) compared to the non-GDE mode (6.6  $\Omega$  cm<sup>-2</sup>). These results highlight the role of HFGDE configuration in facilitating fast electron transfer, improving mass transport and maximizing triplephase interfaces for efficient CO2RR.

To better understand the  $CO_2$  penetrating effect on local  $CO_2$  concentration, computational fluid dynamic (CFD) simulations were performed using the Laminar flow and stationary study (Fig. 3e, f). The simulations illustrate  $CO_2$  velocity and concentration distributions over the HFGDE in both flow-through GDE and non-GDE modes, with the color gradient from red to blue indicating a decrease in  $CO_2$  velocity. In flow-through GDE mode (Fig. 3e), the simulations reveal a high  $CO_2$  concentration at the triple-phase boundary, due to direct delivery of

gaseous  $CO_2$  through the porous tubular wall. Conversely, the non-GDE mode shows significantly lower  $CO_2$  concentration, as the  $CO_2$  supply relies solely on dissolved  $CO_2$  in the electrolyte (Fig. 3f). Admittedly, the  $CO_2$  diffusion pathway is dramatically shortened in flow-through GDE mode, thereby enhancing  $CO_2$  availability and maintaining a sufficient  $CO_2$  supply during the  $CO_2RR$  process. Subsequent  $CO_2RR$  measurements were conducted under flow-through GDE mode.

#### 3.3. CO<sub>2</sub>RR performances of CuBi HFGDEs

The CO<sub>2</sub>RR performances of CuBi HFGDEs with different weight ratios of Bi were evaluated in a three-electrode H-cell (Fig. S2a). From the linear scanning voltammograms (LSVs) of HFGDEs (Fig. 4a), slower increase of current densities at lower potentials (from -0.4 V to -0.8 Vvs. RHE) and faster rise of current densities at higher potentials (from -0.8 V to −1.35 V vs. RHE) where CO<sub>2</sub>RR and hydrogen evolution reaction (HER) occur were observed. CuBi-10 showed the highest current densities among these HFGDEs, attributed to the sufficient Cu/Bi interface in the pore area where a triple-phase region formed during electrocatalysis. Further investigation into the double-layer capacitance (Cdl) (Fig. 4b) of HFGDEs revealed that the Cdl of CuBi-10 was twice as high as that of Cu HFGDEs. CuBi-20 showed the lowest Cdl due to the pore blockage, which led to fewer reactive regions for triple-phase formation. The kinetics of electron transfer was probed by the electrochemical impedance spectroscopy (EIS) at -1.0 V vs RHE (Fig. 4c). CuBi-10 exhibited the smallest arcs size, namely, the lowest charge transfer resistance, indicating CuBi-10 experienced a more efficient catalytic process during CO<sub>2</sub>RR than the other CuBi HFGDEs. The sufficient Cu/Bi interfaces facilitated the electron transfer during CO<sub>2</sub>RR, and resulted in faster electrocatalysis, which is consistent with the results from LSVs.

The selectivity of formate over these HFGDEs was analyzed by chronoamperometry measurements at potentials from -0.7 to -1.2 V vs. RHE with intervals of 0.1 V. Quantitative analysis of liquid and gaseous products verified that formate was the only liquid product while CO and H2 were gaseous products. CuBi HFGDEs exhibited much higher faradaic efficiency (FE) of formate than the pristine Cu HFGDE (Fig. 4d) and effectively suppressed HER (Fig. 4e). Especially CuBi-10 showed the highest FE of formate over 90 % at the potential window of -0.9 V to -1.1 V vs. RHE (Fig. S7), owing to high porosity and sufficient Cu/Bi interfaces in triple-phase regions. The partial current densities of formate (Fig. 4f) indicated that CuBi HFGDEs had higher partial current densities than Cu HFGDE, especially CuBi-10 showed the highest partial current densities at all applied potentials. This could be attributed to both higher formate FE and higher current densities of CuBi HFGDEs. To evaluate the role of Cu/Bi interface in CO2RR, Bi@Cu HF (Bi nanoparticles on Cu HF) with the same surface composition (Fig. S8a and Table S2) and crystal structure (Fig. S8b) as CuBi-10 was tested. Compared to Bi@Cu HF, CuBi-10 showed much higher selectivity for formate production (Fig. S8c) and faster electrocatalytic activity (Fig. S8d), highlighting the superior effect of the intimate Cu/Bi bimetallic interface over the bulk compositional similarity.

To compare the  $\rm CO_2$ -to-formate conversion kinetics of Cu HFGDE and CuBi-10, Tafel slopes were analyzed (Fig. 4g). CuBi-10 showed a lower Tafel slope value than Cu HFGDE, indicating enhanced reaction kinetics attributable to abundant Cu/Bi interfaces at the triple-phase boundaries. The long-term stability of CuBi-10 was first evaluated at -1.0 V vs. RHE (Fig. S9a), which was in the middle of the potential window for the high FE of formate (over 90 %), in the H-cell. CuBi-10 exhibited stable FE of formate (>90 %) for 8 h, then slightly dropped to 88 % after 10 h of operation. This could be attributed to sufficient  $\rm CO_2$  availability on the electrode surface during long-term operation. Moreover, the CuBi-10 retained the crystalline structure after long-term  $\rm CO_2RR$  (Fig. S10a), and post- $\rm CO_2RR$  XPS analysis exhibited no significant changes of Cu 2p and Bi 4f spectra (Fig. S10b, c, d), indicating the chemical stability of CuBi HFGDE during  $\rm CO_2RR$  process. Further

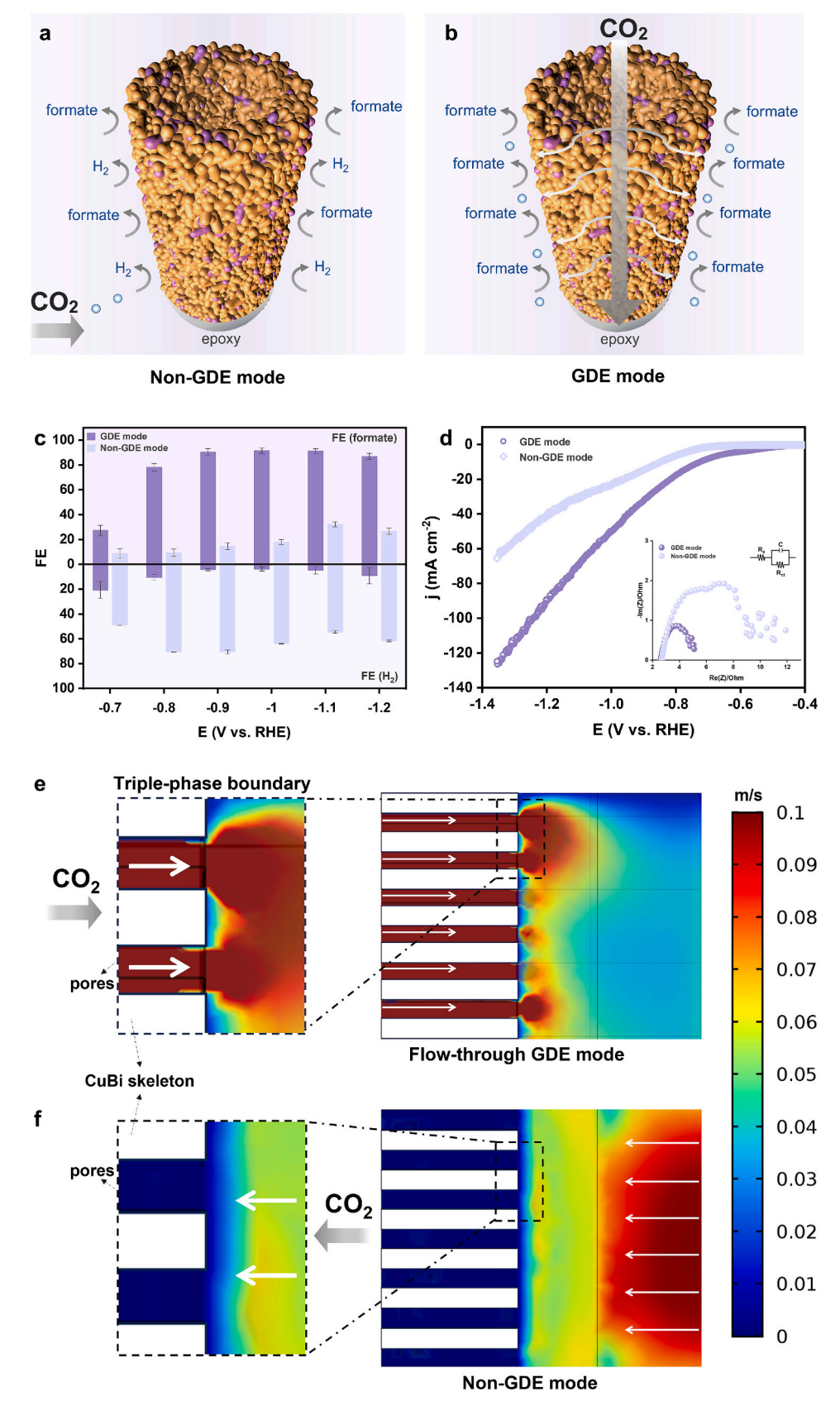


Fig. 3. Schematic of the HFGDE operating in a) non-GDE mode and b) GDE mode; c) FE of formate and  $H_2$  d) linear scanning voltammograms (LSVs) and Nyquist plots (inset figure) of CuBi-10 under two operation modes; Computational fluid dynamic (CFD) modeling the  $CO_2$  distribution in e) flow-through GDE mode and f) non-GDE mode. Arrows show  $CO_2$  stream/diffusion in the schematic of two modes.

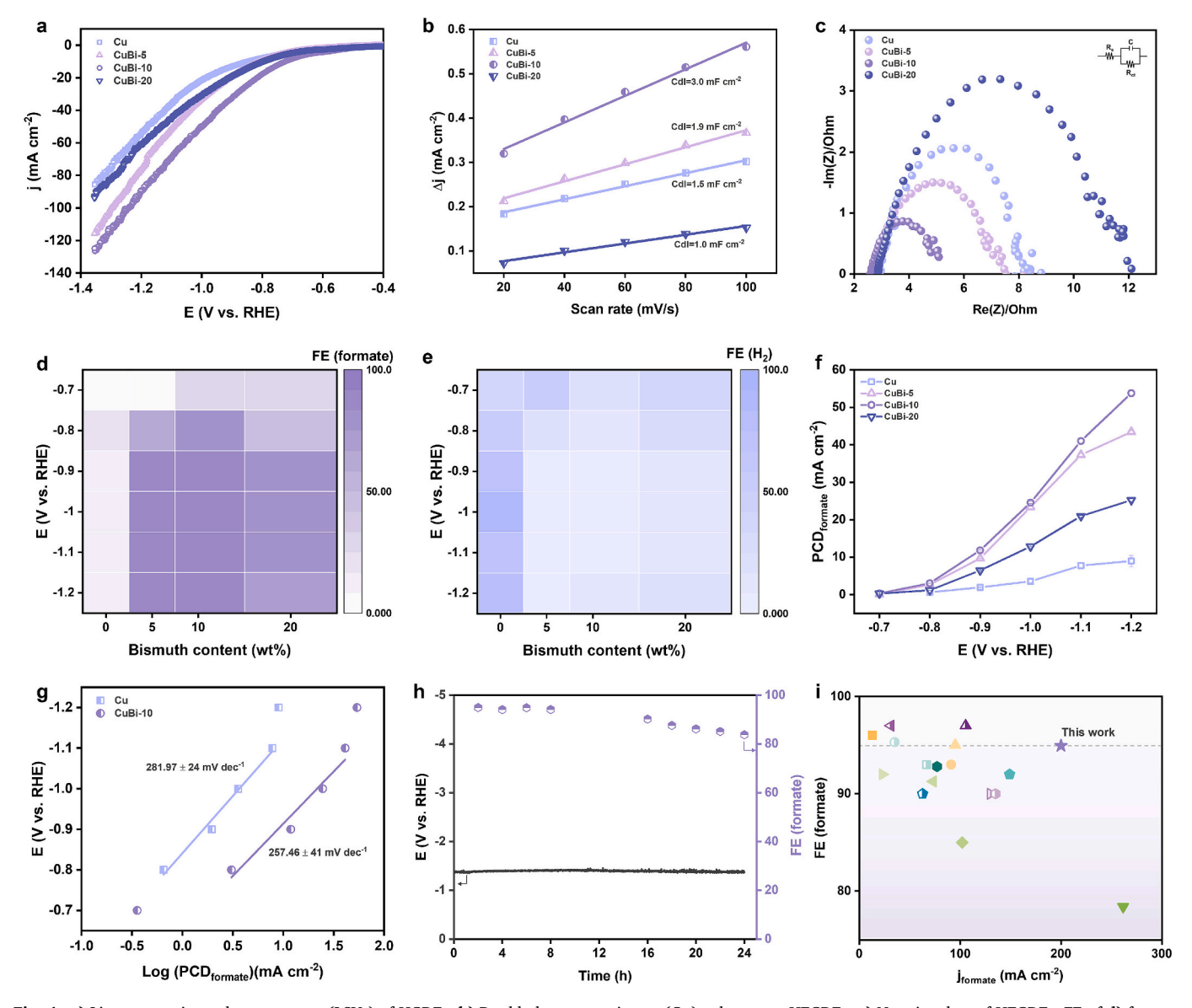


Fig. 4. a) Linear scanning voltammograms (LSVs) of HGDEs; b) Double-layer capacitance ( $C_{dl}$ ) values over HFGDEs; c) Nyquist plots of HFGDEs; FE of d) formate and e)  $H_2$  for HFGDEs with various Bi content; f) partial current densities of formate for HFGDEs; g) Tafel plots of formate for Cu HF and CuBi-10; h) Long-term  $CO_2RR$  performance of CuBi-10 in electrolyte containing 1 M KCl and 0.1 M KHCO<sub>3</sub> at -200 mA cm<sup>-2</sup>; i) Comparison of formate partial current densities and FE of reported Bi-based electrocatalysts for formate production (see Table S4 for further details).

validation of long-term performance at  $-200~\text{mA}~\text{cm}^{-2}$  for 24 h was carried out in 1 M KHCO<sub>3</sub>, the FE of formate decreased to approximately 50 % (Fig. S9b), which can be attributed to enhanced proton availability due to higher KHCO<sub>3</sub> concentration and a relatively limited CO<sub>2</sub> supply at the electrode surface under industrial-level current densities. To suppress HER, potassium chloride (KCl) was introduced into electrolyte, as Cl can effectively suppress competing HER during the CO<sub>2</sub>RR process [55,56]. When CuBi-10 was tested in an electrolyte containing 1 M KCl and 0.1 M KHCO<sub>3</sub> at -200 mA cm<sup>-2</sup>, it exhibited a high FE of formate (>90 %) for 16 h and maintained 83 % after 24 h (Fig. 4h). The observed increase in HER during prolonged operation was due to enhanced hydrophilicity of the electrode surface. SEM and BSE images of the CuBi-10 surface after stability test revealed a rougher but similar morphology with Cu/Bi interfaces on the edge of pores (Fig. S11a, b). Additionally, a decrease in the contact angle was confirmed after the stability test (Fig. S11c, d), indicating a loss of hydrophobicity, which contributed to the increased HER over time. A comparative evaluation of CuBi-10 and other Bi-based electrocatalysts is presented in Fig. 4i and Table S4. Compared to other Bi-based catalysts, CuBi-10 exhibits superior formate partial current density and FE, noting that the method of electrode/catalyst development in this study is scalable, unlike most studies with complex synthesis procedures.

Electrolytes significantly affect the reaction kinetics and product selectivity of CO2RR, as these properties are influenced by CO2 solubility, ionic conductivity, local pH, cation effects and electrolyte-catalyst interfaces [57-60]. To comprehend the impact of electrolyte concentration, further investigations of the CO<sub>2</sub>RR performance of CuBi-10 in 1 M and 2 M KHCO<sub>3</sub> were carried out (Fig. S12). As the KHCO<sub>3</sub> concentration increased, current densities rose correspondingly (Fig. S12a), while the charge transfer resistance significantly decreased (Fig. S12b), owing to enhanced electrolyte conductivity. Formate selectivity was reduced while HER became dominant when increasing KHCO3 concentration to 2 M (Fig. S12c, d). This is mainly due to the insufficient CO2 supply on the electrode surface under high current densities (more than 4 times higher in 2 M KHCO<sub>3</sub> solution than that in 0.5 M KHCO<sub>3</sub> at -1.0V vs. RHE), and stronger proton donation from more concentrated KHCO3. Additionally, the pH increased slightly at higher KHCO3 concentrations (Table S1), resulting in lower CO2 solubility [61], which led

to decreased formate selectivity.

#### 3.4. Mechanism study of CO2RR on Cu/Bi interface

To reveal the fundamental mechanism and gain deeper insights into CO<sub>2</sub>RR on Cu/Bi interface, in-situ Raman spectroscopy was conducted on CuBi-10, CuBi-20 and Cu HF. To examine the evolution of Bi, in-situ Raman spectra were recorded by sequential application of potentials from open circuit potential (OCP) to -0.8 V vs. RHE (Figs. 5a and S13a) and within continuous 1200s at -0.6 V vs. RHE (Figs. 5b and S13b). The slight peaks at 142 and 166 cm<sup>-1</sup>, corresponding to Bi-O bond, were observed at OCP and then disappeared when potential was applied. While the characteristic peaks of  $E_g$  and  $A_{1g}$  modes of metallic Bi at 71 and 98 cm<sup>-1</sup> [62] maintained dominance in both potential-dependent and time-dependent Raman spectra, indicating that the inevitable Bi<sub>2</sub>O<sub>3</sub> on the electrode surface (when exposed to air) was instantly reduced to metallic Bi during CO<sub>2</sub>RR. Moreover, an additional peak of (BiO)<sub>2</sub>CO<sub>3</sub> at 187 cm<sup>-1</sup> became obvious from -0.2 V vs. RHE onwards (Figs. 5a and S13a) and from 40s (Figs. 5b and S13b), suggesting CO<sub>2</sub> adsorption on Cu/Bi interface in CO<sub>2</sub>RR process [63,64].

In-situ Raman spectra were additionally employed to detect the possible intermediates on Cu/Bi interface during  $CO_2RR$ . In general,  $CO_2$  can be reduced to formate in two pathways. One way is through \*COOH (carboxylate radical) intermediate, and the other way is via \*OCHO (formate). The \*OCHO pathway is significantly in downhill energy on Cu/Bi interface when compared with \*COOH pathway [65], which means the \*OCHO pathway is more energetically favorable for the

conversion of CO2 to formate. In-situ Raman results confirmed this (Figs. 5c, d and S13c). The intrinsic peaks at about 1361 and 1645 cm<sup>-1</sup> contributing to HCO<sub>3</sub> and H<sub>2</sub>O molecules [66,67] were initially identified, and as compared to Cu HF (Fig. 5d), the emerging peak at 1450 cm<sup>-1</sup> for \*OCHO [68,69] from -0.5 V vs. RHE was recognized on CuBi-10 (Fig. 5c) in the CO<sub>2</sub>-to-formate process. Moreover, in the \*COOH pathway, \*CO<sup>-</sup> can be formed to generate CO or C<sub>2+</sub> products [70], yet no C<sub>2+</sub> products and only trace amounts of CO were detected in this work, so C-C coupling did not occur and the \*COOH pathway was not the dominant one. Therefore, Cu/Bi interface in the three-phase boundary can effectively favor the \*OCHO pathway and hinder the \*COOH pathway (as shown in Fig. 5f), thus improving the selectivity of formate. Furthermore, Raman spectra from  $600 \text{ to } 1000 \text{ cm}^{-1}$  for Cu HF, CuBi-10 and CuBi-20 (Fig. 5e) were compared to evaluate the hydrogen adsorption on the Cu/Bi interface. A prominent peak at 804 cm<sup>-1</sup>, attributed to vCu-H from copper-hydrogen interactions [71], was observed in Cu HF, leading to its high H2 FE. In contrast, CuBi-10 and CuBi-20 hardly showed the vCu-H signals, indicating suppressed HER on Cu/Bi interface. These findings are consistent with the results shown in Fig. 4e.

#### 4. Conclusion

In this study, bimetallic HFGDEs with abundant Cu/Bi interfaces were prepared through a facile approach to promote the selective generation of formate for CO<sub>2</sub>RR. Premixing metal sources enables a uniform distribution of Bi-phase within the Cu skeleton of HFGDEs,

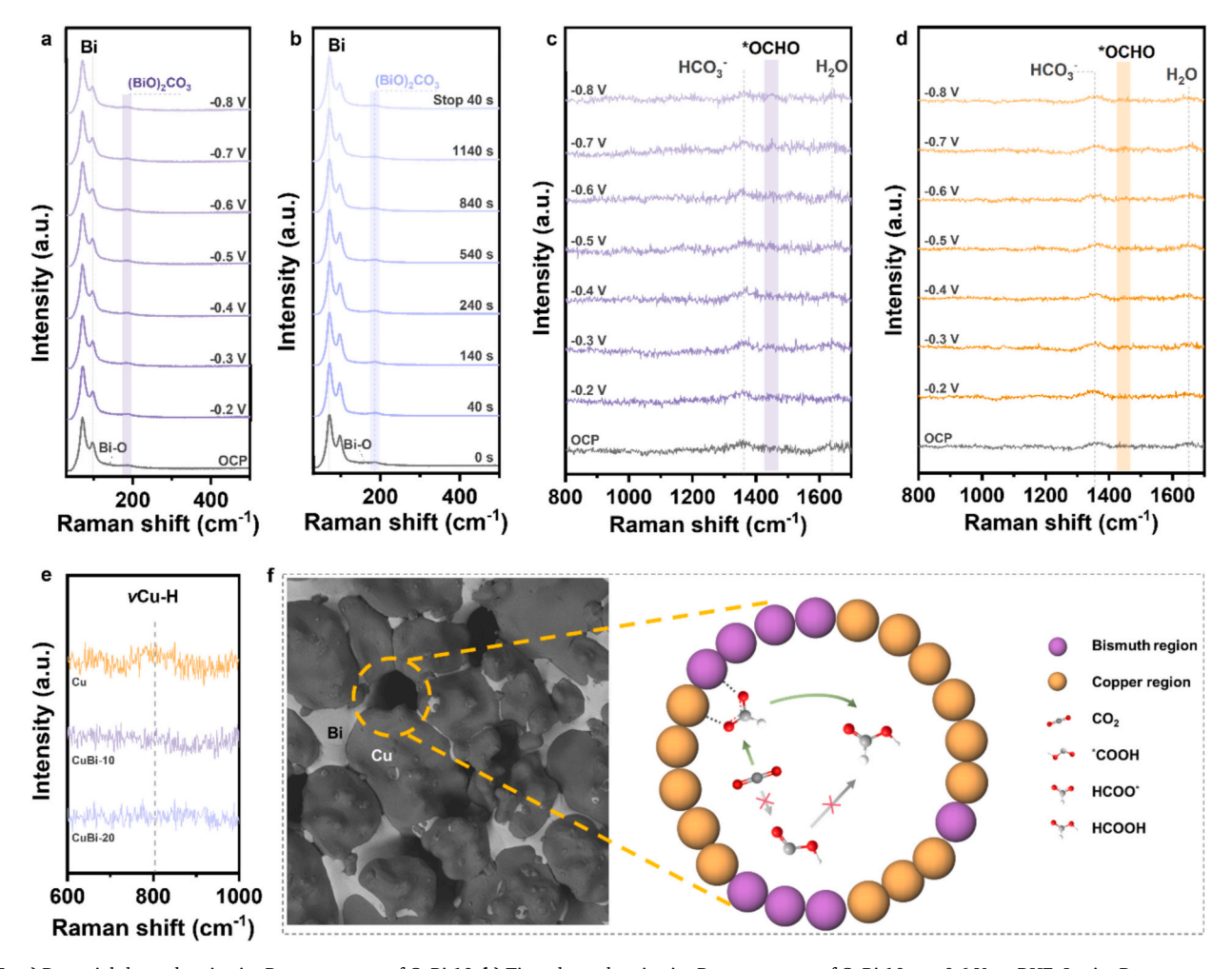


Fig. 5. a) Potential-dependent in-situ Raman spectra of CuBi-10; b) Time-dependent in-situ Raman spectra of CuBi-10 at -0.6 V vs. RHE; In-situ Raman spectra of c) CuBi-10 and d) Cu HF at various potentials; e) Raman spectra of CO<sub>2</sub>RR on HFGDEs at -0.7 V vs. RHE; f) schematic of CO<sub>2</sub>-to-formate pathway on Cu/Bi interface.

facilitating the formation of Cu/Bi interfaces at the triple-phase boundary at the edges of the accessible pores during CO2RR. CuBi HFGDEs with an optimal Bi weight ratio (10 wt%) exhibited an ideal proportion of Cu/Bi interface located at the edges of pores, while maintaining the overall porosity of HFGDEs. The CuBi-10 operated in flow-through GDE mode effectively suppressed HER and achieved much higher selectivity over formate than in non-GDE mode. This highlights the importance of HFGDE architecture in ensuring sufficient CO<sub>2</sub> at the triple-phase boundaries. CuBi-10 showed the highest formate selectivity, with a Faradaic efficiency greater than 90 % over a low potential range from -0.9 V to -1.1 V vs. RHE, and fastest reaction kinetics regarding current density, active sites and charge transfer resistance, outperformed Cu HFGDEs, owing to sufficient Cu/Bi interfaces at triplephase boundaries. Furthermore, in-situ Raman revealed that the Cu/Bi interface can effectively suppress HER and favor the \*OCHO pathway during CO2-to-formate reduction. This research demonstrated the potential of engineering metal-based gas-diffusion electrodes for formate production via designing bimetallic interfaces at triple-phase boundaries with microtubular architecture.

#### CRediT authorship contribution statement

Beibei Ma: Writing – review & editing, Writing – original draft, Visualization, Validation, Methodology, Investigation, Formal analysis, Data curation. Hesamoddin Rabiee: Writing – review & editing, Writing – original draft, Methodology, Investigation, Funding acquisition, Formal analysis. Guoliang Chen: Writing – original draft, Investigation, Formal analysis, Data curation. Yizhu Kuang: Formal analysis, Data curation. Tianjiu Zhu: Formal analysis, Data curation. Penghui Yan: Formal analysis, Data curation. Lei Ge: Writing – review & editing, Writing – original draft, Supervision, Resources, Project administration, Methodology, Investigation, Funding acquisition, Conceptualization. Zhonghua Zhu: Writing – review & editing, Validation, Supervision, Resources, Project administration, Investigation, Funding acquisition, Conceptualization.

# Declaration of competing interest

The authors declare that they have no known competing financial interests or personal relationships that could have appeared to influence the work reported in this paper.

# Acknowledgements

We acknowledge financial support from the ARC Future Fellowship (FT220100166) and Centre of Excellence for Green Electrochemical Transformation of Carbon Dioxide (CE230100017). Dr Hesamoddin Rabiee acknowledges SNSF Swiss Postdoctoral Fellowship (217305). We acknowledge the facilities and technical assistance of Quantitative and Multi-omics Analysis Platform (Q-MAP) and National Collaborative Research Infrastructure Strategy (NCRIS) at the University of Queensland (UQ) and the AWMC Analytical Services Laboratory (ASL) for HPLC tests. We acknowledge the support from the Centre for Microscopy and Microanalysis (CMM) at UQ for SEM, TEM, XRD, and XPS analysis.

#### Appendix A. Supplementary data

Supplementary data to this article can be found online at https://doi.org/10.1016/j.cej.2025.168323.

#### Data availability

All data supporting the findings of this study are included within the article and its Supplementary Information.

#### References

- [1] X. Wang, Z. Wang, F.P. García de Arquer, C.-T. Dinh, A. Ozden, Y.C. Li, D.-H. Nam, J. Li, Y.-S. Liu, J. Wicks, Z. Chen, M. Chi, B. Chen, Y. Wang, J. Tam, J.Y. Howe, A. Proppe, P. Todorović, F. Li, T.-T. Zhuang, C.M. Gabardo, A.R. Kirmani, C. McCallum, S.-F. Hung, Y. Lum, M. Luo, Y. Min, A. Xu, C.P. O'Brien, B. Stephen, B. Sun, A.H. Ip, L.J. Richter, S.O. Kelley, D. Sinton, E.H. Sargent, Efficient electrically powered CO2-to-ethanol via suppression of deoxygenation, Nat. Energy 5 (6) (2020) 478–486, https://doi.org/10.1038/s41560-020-0607-8.
- [2] C. Xu, Y. Dong, H. Zhao, Y. Lei, CO2 conversion toward real-world applications: electrocatalysis versus CO2 batteries, Adv. Funct. Mater. 33 (32) (2023) 2300926, https://doi.org/10.1002/adfm.202300926.
- [3] Y. Kuang, H. Rabiee, L. Ge, T.E. Rufford, Z. Yuan, J. Bell, H. Wang, High-concentration electrosynthesis of formic acid/formate from CO2: reactor and electrode design strategies, Energy Environ. Mater. 6 (6) (2023) e12596, https://doi.org/10.1002/epm2.12596.
- [4] H. Rabiee, A. Dutta, P. Yan, L. Ge, F. Dorosti, X. Yu, A. Rieder, P. Broekmann, Broekmann, From flue gas to syngas: composite electrode based on ionic liquid and microporous polymer for MEA-based CO2 electrolysis, Angew. Chem. Int. Ed. (2025) e202513103, https://doi.org/10.1002/anie.202513103.
- [5] C. Chen, J.F. Khosrowabadi Kotyk, S.W. Sheehan, Progress toward commercial application of electrochemical carbon dioxide reduction, Chem 4 (11) (2018) 2571–2586. https://doi.org/10.1016/j.chempr.2018.08.019.
- [6] T. Zheng, C. Liu, C. Guo, M. Zhang, X. Li, Q. Jiang, W. Xue, H. Li, A. Li, C.-W. Pao, J. Xiao, C. Xia, J. Zeng, Copper-catalysed exclusive CO2 to pure formic acid conversion via single-atom alloying, Nat. Nanotechnol. 16 (12) (2021) 1386–1393, https://doi.org/10.1038/s41565-021-00974-5.
- [7] Q. Lu, H. Xiong, D. Wu, R. Jiang, H. Li, Q. Hu, X. Lu, B. Xu, Sustainable synthesis of concentrated formate via CO2 electrolysis integrated with Cl2 formation, Angew. Chem. Int. Ed. 64 (2025) e202504782. https://doi.org/10.1002/anje.202504782.
- [8] B. Li, J. Chen, L. Wang, D. Xia, S. Mao, L. Xi, S. Ying, H. Zhang, Y. Wang, Dynamic reconstruction of Cu-doped SnO2 for efficient electrochemical reduction of CO2 to formate, Appl. Catal. B Environ. Energy 363 (2025) 124784, https://doi.org/ 10.1016/j.apcatb.2024.124784.
- [9] H. Rabiee, L. Ge, X. Zhang, S. Hu, M. Li, S. Smart, Z. Zhu, H. Wang, Z. Yuan, Standalone asymmetric hollow fiber gas-diffusion electrodes with distinguished bronze phases for high-efficiency CO2 electrochemical reduction, Appl. Catal. B Environ. 298 (2021) 120538, https://doi.org/10.1016/j.apcatb.2021.120538.
- [10] T. Yan, X. Chen, L. Kumari, J. Lin, M. Li, Q. Fan, H. Chi, T.J. Meyer, S. Zhang, X. Ma, Multiscale CO2 electrocatalysis to C2+ products: reaction mechanisms, catalyst design, and device fabrication, Chem. Rev. 123 (17) (2023) 10530–10583, https://doi.org/10.1021/acs.chemrev.2c00514.
- [11] N.H. Tran, M.W. Schreiber, M. Fontecave, Catalysts for selective CO2/CO electroreduction to C3+ compounds, EES Catal. (2025), https://doi.org/10.1039/ D5EY00047E
- [12] S.J. Raaijman, M.P. Schellekens, Y.J. Son, M.T.M. Koper, P.J. Corbett, Identification of catalyst optimization trends for electrocatalytic CO(2) reduction to ethylene, EES Catal. 3 (3) (2025) 386–406, https://doi.org/10.1039/ D4FV00287C
- [13] S. Kong, X. Lv, J. Wang, Effects of the delocalization state on electrocatalytic CO2 reduction: a mini-review, EES Catal. 2 (2) (2024) 556–563, https://doi.org/ 10.1039/D3FY00227F
- [14] H. Rabiee, M. Li, P. Yan, Y. Wu, X. Zhang, F. Dorosti, X. Zhang, B. Ma, S. Hu, H. Wang, Z. Zhu, L. Ge, Rational designing microenvironment of gas-diffusion electrodes via microgel-augmented CO2 availability for high-rate and selective CO2 electroreduction to ethylene, Adv. Sci. 11 (40) (2024) 2402964, https://doi.org/10.1002/advs.202402964.
- [15] H. Rabiee, L. Ge, X. Zhang, S. Hu, M. Li, Z. Yuan, Gas diffusion electrodes (GDEs) for electrochemical reduction of carbon dioxide, carbon monoxide, and dinitrogen to value-added products: a review, Energy Environ. Sci. 14 (4) (2021) 1959–2008, https://doi.org/10.1039/D0EE03756G.
- [16] H. Rabiee, B. Ma, Y. Yang, F. Li, P. Yan, Y. Wu, X. Zhang, S. Hu, H. Wang, L. Ge, Z. Zhu, Advances and challenges of carbon-free gas-diffusion electrodes (GDEs) for electrochemical CO2 reduction, Adv. Funct. Mater. 35 (1) (2025) 2411195, https://doi.org/10.1002/adfm.202411195
- [17] H.-P. Iglesias van Montfort, M. Li, E. Irtem, M. Abdinejad, Y. Wu, S.K. Pal, M. Sassenburg, D. Ripepi, S. Subramanian, J. Biemolt, T.E. Rufford, T. Burdyny, Non-invasive current collectors for improved current-density distribution during CO2 electrolysis on super-hydrophobic electrodes, Nat. Commun. 14 (1) (2023) 6579, https://doi.org/10.1038/s41467-023-42348-6.
- [18] L.M. Baumgartner, A. Goryachev, C.I. Koopman, D. Franzen, B. Ellendorff, T. Turek, D.A. Vermaas, Electrowetting limits electrochemical CO 2 reduction in carbon-free gas diffusion electrodes, Energy Adv. 2 (11) (2023) 1893–1904.
- [19] S. Yamaguchi, H. Ebe, T. Minegishi, M. Sugiyama, Introduction of a conductive layer into flood-resistant gas diffusion electrodes with polymer substrate for an efficient electrochemical CO2 reduction with copper oxide, ACS Appl. Mater. Interfaces 16 (14) (2024) 17371–17376, https://doi.org/10.1021/ acsami.3c14568.
- [20] M. Sun, J. Cheng, M. Yamauchi, Gas diffusion enhanced electrode with ultrathin superhydrophobic macropore structure for acidic CO2 electroreduction, Nat. Commun. 15 (1) (2024) 491, https://doi.org/10.1038/s41467-024-44722-4.
- [21] A.H. da Silva, S.J. Raaijman, P.J. Corbett, Mesh GDEs: an alternative to carbon-based electrodes for CO<sub>2</sub> reduction at higher current densities, Chem. Eng. J. 494 (2024) 153266.
- [22] K. Mishra, N. Devi, S.S. Siwal, V.K. Thakur, Insight perspective on the synthesis and morphological role of the noble and non-noble metal-based electrocatalyst in fuel

- cell application, Appl. Catal. B Environ. 334 (2023) 122820, https://doi.org/
- [23] H. Rabiee, L. Ge, S. Hu, H. Wang, Z. Yuan, Microtubular electrodes: an emerging electrode configuration for electrocatalysis, bioelectrochemical and water treatment applications, Chem. Eng. J. 450 (2022) 138476, https://doi.org/ 10.1016/j.cej.2022.138476.
- [24] G. Chen, L. Ge, Y. Kuang, H. Rabiee, B. Ma, F. Dorosti, A. Kumar Nanjundan, Z. Zhu, H. Wang, Hollow fiber gas-diffusion electrodes with tailored crystal facets for tuning syngas production in electrochemical CO2 reduction, Chem. Eng. J. 490 (2024) 151651, https://doi.org/10.1016/j.cej.2024.151651.
- [25] H. Rabiee, L. Ge, X. Zhang, S. Hu, M. Li, S. Smart, Z. Zhu, Z. Yuan, Shape-tuned electrodeposition of bismuth-based nanosheets on flow-through hollow fiber gas diffusion electrode for high-efficiency CO2 reduction to formate, Appl. Catal. B Environ. 286 (2021) 119945, https://doi.org/10.1016/j.apcatb.2021.119945.
- [26] G. Chen, L. Ge, Y. Kuang, H. Rabiee, B. Ma, F. Dorosti, A.K. Nanjundan, Z. Zhu, H. Wang, In situ growth of hierarchical silver sub-nanosheets on zinc nanosheets-based hollow fiber gas-diffusion electrodes for electrochemical CO2 reduction to CO, Small Sci. 4 (10) (2024) 2400184, https://doi.org/10.1002/smsc.202400184.
- [27] H. Rabiee, X. Zhang, L. Ge, S. Hu, M. Li, S. Smart, Z. Zhu, Z. Yuan, Tuning the product selectivity of the cu hollow fiber gas diffusion electrode for efficient CO2 reduction to formate by controlled surface sn electrodeposition, ACS Appl. Mater. Interfaces 12 (19) (2020) 21670–21681, https://doi.org/10.1021/acsami.0c03681
- [28] Y. Xia, Z. Meng, Z. Zhang, F. Wang, S. Min, Interfacing dense NiFe@N-doped carbon nanotubes on a Ni hollow fiber as a high-current-density gas-penetrable electrode for selective CO2 electroreduction, Energy Fuel 38 (9) (2024) 8062–8071, https://doi.org/10.1021/acs.energyfuels.4c00477.
- [29] G. Chen, L. Ge, B. Ma, Y. Kuang, H. Rabiee, F. Dorosti, A.K. Nanjundan, Z. Zhu, H. Wang, Pore accessibility matters in CO2 electrolysis: preventing H2 formation and boosting triple-phase boundary on microtubular gas-diffusion electrodes, Appl. Catal. B Environ. Energy 363 (2025) 124803, https://doi.org/10.1016/j.apcatb.2024.124803.
- [30] H. Rabiee, J.K. Heffernan, L. Ge, X. Zhang, P. Yan, E. Marcellin, S. Hu, Z. Zhu, H. Wang, Z. Yuan, Tuning flow-through Cu-based hollow fiber gas-diffusion electrode for high-efficiency carbon monoxide (CO) electroreduction to C2+products, Appl. Catal. B Environ. 330 (2023) 122589, https://doi.org/10.1016/j.apcath.2023.122589
- [31] Y. Kuang, G. Chen, D.H. Mudiyanselage, H. Rabiee, B. Ma, F. Dorosti, A. K. Nanjundan, Z. Zhu, H. Wang, L. Ge, Engineering interfacial molecular interactions on Ag hollow fibre gas diffusion electrodes for high efficiency in CO<sub>2</sub> conversion to CO, Chem. Eur. J. 30 (72) (2024) e202403251, https://doi.org/10.1002/chem.202403251.
- [32] Y. Kuang, G. Chen, H. Rabiee, B. Ma, F. Dorosti, A.K. Nanjundan, Z. Zhu, H. Wang, L. Ge, Steering CO selectivity in CO2 electroreduction over silver microtubular gasdiffusion electrodes via surface reconstruction, Energy Fuel 38 (11) (2024) 10096–10105, https://doi.org/10.1021/acs.energyfuels.4c01240.
- [33] C. Zhu, G. Wu, J. Mao, A. Chen, Y. Zhao, G. Feng, Y. Wei, X. Liu, S. Li, G. Li, X. Dong, Y. Song, W. Wei, W. Chen, Halide-modulated hollow-fiber Cu penetration electrode boosts Ampere-level CO2 electroreduction to multicarbon products, Chem. Eng. J. 485 (2024) 150040. https://doi.org/10.1016/j.cej.2024.150040.
- [34] S. Li, X. Dong, G. Wu, Y. Song, J. Mao, A. Chen, C. Zhu, G. Li, Y. Wei, X. Liu, J. Wang, W. Chen, W. Wei, Ampere-level CO2 electroreduction with single-pass conversion exceeding 85% in acid over silver penetration electrodes, Nat. Commun. 15 (1) (2024) 6101, https://doi.org/10.1038/s41467-024-50521-8.
- [35] A. Chen, C. Zhu, J. Mao, S. Li, G. Wu, Y. Wei, X. Liu, X. Dong, Y. Song, G. Li, Y. Sun, W. Wei, W. Chen, Hollow penetration electrode of Bi with dislocated lattice enabling ampere-level reduction of CO2 exclusively to formate, Appl. Catal. B Environ. 343 (2024) 123493, https://doi.org/10.1016/j.apcatb.2023.123493.
- [36] G. Chen, H. Rabiee, M. Li, B. Ma, Y. Kuang, F. Dorosti, Z. Zhu, H. Wang, L. Ge, Engineering flow-through hollow fiber gas-diffusion electrodes for unlocking highrate gas-phase electrochemical conversion, Adv. Mater. 37 (2025) 2420391, https://doi.org/10.1002/adma.202420391.
- [37] K.P. Kuhl, E.R. Cave, D.N. Abram, T.F. Jaramillo, New insights into the electrochemical reduction of carbon dioxide on metallic copper surfaces, Energy Environ. Sci. 5 (5) (2012) 7050–7059, https://doi.org/10.1039/C2EE21234J.
- [38] C. Qin, X. Li, T. Wang, Z. Xu, K.-J. Chen, F. Pan, Metal-organic frameworks-based copper catalysts for CO2 electroreduction toward multicarbon products, Exploration 5 (3) (2025) 270011, https://doi.org/10.1002/EXP.70011.
- [39] C.W. Lee, K.D. Yang, D.-H. Nam, J.H. Jang, N.H. Cho, S.W. Im, K.T. Nam, Defining a materials database for the design of copper binary alloy catalysts for electrochemical CO2 conversion, Adv. Mater. 30 (42) (2018) 1704717, https://doi. org/10.1002/adma.201704717
- [40] X. Gao, Y. Jiang, J. Liu, G. Shi, C. Yang, Q. Xu, Y. Yun, Y. Shen, M. Chang, C. Zhu, T. Lu, Y. Wang, G. Du, S. Li, S. Dai, L. Zhang, Intermediate-regulated dynamic restructuring at Ag-Cu biphasic interface enables selective CO2 electroreduction to C2+ fuels, Nat. Commun. 15 (1) (2024) 10331, https://doi.org/10.1038/s41467-024\_E4620.2
- [41] J. Gu, S. Liu, W. Ni, W. Ren, S. Haussener, X. Hu, Modulating electric field distribution by alkali cations for CO2 electroreduction in strongly acidic medium, Nat. Catal. 5 (4) (2022) 268–276, https://doi.org/10.1038/s41929-022-00761-y.
- [42] M. Zhang, Z. Zhang, Z. Zhao, H. Huang, D.H. Anjum, D. Wang, J.-h. He, K.-W. Huang, Tunable selectivity for electrochemical CO2 reduction by bimetallic Cu-Sn catalysts: elucidating the roles of Cu and Sn, ACS Catal. 11 (17) (2021) 11103–11108, https://doi.org/10.1021/acscatal.1c02556.
- [43] H. Li, X. Yue, J. Che, Z. Xiao, X. Yu, F. Sun, C. Xue, J. Xiang, High performance 3D self-supporting Cu–Bi aerogels for electrocatalytic reduction of CO2 to formate,

- ChemSusChem 15 (7) (2022) e202200226, https://doi.org/10.1002/
- [44] L. Lu, X. Sun, J. Ma, D. Yang, H. Wu, B. Zhang, J. Zhang, B. Han, Highly efficient electroreduction of CO2 to methanol on palladium-copper bimetallic aerogels, Angew. Chem. 130 (43) (2018) 14345–14349.
- [45] H. Yang, H. Chuai, Q. Meng, M. Wang, S. Zhang, X. Ma, Copper-based bimetallic electrocatalysts for CO2 reduction: From mechanism understandings to product regulations, Mater. Rep.: Energy 3 (1) (2023) 100174, https://doi.org/10.1016/j. matre.2022.100174.
- [46] P.-F. Sui, M.-R. Gao, M.-N. Zhu, C. Xu, Y.-C. Wang, S. Liu, J.-L. Luo, Unlocking nanotubular bismuth oxyiodide toward carbon-neutral electrosynthesis, EES Catal. 1 (3) (2023) 290–300, https://doi.org/10.1039/D3EY00034F.
- [47] X.-D. Liang, N. Tian, S.-N. Hu, Z.-Y. Zhou, S.-G. Sun, Recent advances of bismuth-based electrocatalysts for CO2 reduction: strategies, mechanism and applications, Mater. Rep.: Energy 3 (2) (2023) 100191, https://doi.org/10.1016/j.psptra.2023.101101
- [48] Y. Hao, Y. Cheng, J. Wang, K. Wang, Z. Chen, H. Wang, F. Li, M. Huang, Q. Zhang, X. Zhao, Chlorine-vacancy-mediated electronic modulation in bismuth oxychloride on porous graphene: unlocking high-efficiency CO2 electroreduction to formate, Appl. Catal. B Environ. Energy 376 (2025) 125472, https://doi.org/10.1016/j. apcatb.2025.125472.
- [49] Z. Zhang, W. Liu, W. Zhang, M. Liu, S. Huo, Interface interaction in CuBi catalysts with tunable product selectivity for electrochemical CO2 reduction reaction, Colloids Surf. A Physicochem. Eng. Asp. 631 (2021) 127637, https://doi.org/ 10.1016/j.colsurfa.2021.127637.
- [50] Z. Yang, H. Wang, X. Fei, W. Wang, Y. Zhao, X. Wang, X. Tan, Q. Zhao, H. Wang, J. Zhu, MOF derived bimetallic CuBi catalysts with ultra-wide potential window for high-efficient electrochemical reduction of CO2 to formate, Appl. Catal. B Environ. 298 (2021) 120571.
- [51] W. Li, J. Hong, J. Shang, H. Yamashita, C. Wei, Y. Hu, In situ construction of CuBi-MOF derived heterojunctions with electron-rich effects enhances localized CO2 enrichment integrated with Si photocathodes for CO2 reduction, Appl. Catal. B Environ. Energy 365 (2025) 124890.
- [52] T. Shi, D. Liu, H. Feng, Y. Zhang, Q. Li, Evolution of triple-phase interface for enhanced electrochemical CO2 reduction, Chem. Eng. J. 431 (2022) 134348, https://doi.org/10.1016/j.cej.2021.134348.
- [53] G. He, S. Huang, L.F. Villalobos, J. Zhao, M. Mensi, E. Oveisi, M. Rezaei, K. V. Agrawal, High-permeance polymer-functionalized single-layer graphene membranes that surpass the postcombustion carbon capture target, Energy Environ. Sci. 12 (11) (2019) 3305–3312, https://doi.org/10.1039/C9EE01238A.
- [54] P. Deng, H. Wang, R. Qi, J. Zhu, S. Chen, F. Yang, L. Zhou, K. Qi, H. Liu, B.Y. Xia, Bismuth oxides with enhanced bismuth-oxygen structure for efficient electrochemical reduction of carbon dioxide to formate, ACS Catal. 10 (1) (2020) 743–750, https://doi.org/10.1021/acscatal.9b04043.
- [55] S. Li, X. Dong, Y. Zhao, J. Mao, W. Chen, A. Chen, Y. Song, G. Li, Z. Jiang, W. Wei, Y. Sun, Chloride ion adsorption enables Ampere-level CO2 electroreduction over silver hollow fiber, Angew. Chem. Int. Ed. 61 (42) (2022) e202210432, https://doi.org/10.1002/anje.202210432
- [56] H. Farahmandazad, S. Asperti, R. Kortlever, E. Goetheer, W. de Jong, Effect of halide anions on electrochemical CO2 reduction in non-aqueous choline solutions using Ag and Au electrodes, ChemistryOpen 13 (11) (2024) e202400166, https://doi.org/10.1002/open.202400166.
- [57] Y. Zhou, K. Wang, S. Zheng, X. Cheng, Y. He, W. Qin, X. Zhang, H. Chang, N. Zhong, X. He, Advancements in electrochemical CO2 reduction reaction: a review on CO2 mass transport enhancement strategies, Chem. Eng. J. 486 (2024) 150169, https://doi.org/10.1016/j.cej.2024.150169.
- [58] Y. An, Y. Lee, Y. Ji, Y.D. Kim, H.O. Seo, D.-Y. Jung, CO2 reduction efficiency through electrolyte immersion in hierarchical bismuth-nickel catalysts, Dalton Trans. 53 (45) (2024) 18346–18354, https://doi.org/10.1039/D4DT02441A.
- [59] F. Zeng, B. Pan, L. Wang, Y. Li, Y. Wang, On the role of electrolyte flow in Cucatalyzed CO2 and CO electroreduction, Nano Energy 131 (2024) 110201, https:// doi.org/10.1016/j.nanoen.2024.110201.
- [60] D. Gao, R.M. Arán-Ais, H.S. Jeon, B. Roldan Cuenya, Rational catalyst and electrolyte design for CO2 electroreduction towards multicarbon products, Nat. Catal. 2 (3) (2019) 198–210, https://doi.org/10.1038/s41929-019-0235-5.
- [61] W. Chen, X. Du, S. Tao, B. Lin, I. Tranca, F. Tielens, M. Ma, Z. Liu, Electrolyte effects on reaction kinetics in electrochemical CO2 reduction: the roles of pH, cations, and anions, Chem. Phys. Rev. 6 (1) (2025), https://doi.org/10.1063/5.0242304
- [62] F. Yang, A.O. Elnabawy, R. Schimmenti, P. Song, J. Wang, Z. Peng, S. Yao, R. Deng, S. Song, Y. Lin, Bismuthene for highly efficient carbon dioxide electroreduction reaction, Nat. Commun. 11 (1) (2020) 1088.
- [63] Y. Liu, Z. Wei, X. Su, X. Shi, L. Liu, T. Wang, X. Xu, M. Zhao, Y. Zhai, H.B. Yang, Promoting electrochemical CO2 reduction to formate via sulfur-assisted electrolysis, Adv. Funct. Mater. 35 (21) (2025) 2403547.
- [64] A. Dutta, I. Zelocualtecatl Montiel, K. Kiran, A. Rieder, V. Grozovski, L. Gut, P. Broekmann, A tandem (Bi2O3 → Bimet) catalyst for highly efficient ec-CO2 conversion into formate: operando Raman spectroscopic evidence for a reaction pathway change, ACS Catal. 11 (9) (2021) 4988–5003, https://doi.org/10.1021/ pegestal.0.05517.
- [65] Z. Yang, H. Wang, X. Fei, W. Wang, Y. Zhao, X. Wang, X. Tan, Q. Zhao, H. Wang, J. Zhu, L. Zhou, H. Ning, M. Wu, MOF derived bimetallic CuBi catalysts with ultrawide potential window for high-efficient electrochemical reduction of CO2 to formate, Appl. Catal. B Environ. 298 (2021) 120571, https://doi.org/10.1016/j.apcatb.2021.120571.

- [66] X. Chen, J. Chen, N.M. Alghoraibi, D.A. Henckel, R. Zhang, U.O. Nwabara, K. E. Madsen, P.J.A. Kenis, S.C. Zimmerman, A.A. Gewirth, Electrochemical CO2-to-ethylene conversion on polyamine-incorporated Cu electrodes, Nat. Catal. 4 (1) (2021) 20–27, https://doi.org/10.1038/s41929-020-00547-0.
- [67] W. Shan, R. Liu, H. Zhao, Z. He, Y. Lai, S. Li, G. He, J. Liu, In situ surface-enhanced Raman spectroscopic evidence on the origin of selectivity in CO2 electrocatalytic reduction, ACS Nano 14 (9) (2020) 11363–11372, https://doi.org/10.1021/ acsnano.0c03534.
- [68] D. Bohra, I. Ledezma-Yanez, G. Li, W. de Jong, E.A. Pidko, W.A. Smith, Lateral adsorbate interactions inhibit HCOO— while promoting CO selectivity for CO2 electrocatalysis on silver, Angew. Chem. Int. Ed. 58 (5) (2019) 1345–1349, https://doi.org/10.1002/anie.201811667.
- [69] T. Shi, D. Liu, N. Liu, Y. Zhang, H. Feng, Q. Li, Triple-phase interface engineered hierarchical porous electrode for CO2 electroreduction to formate, Adv. Sci. 9 (30) (2022) 2204472.
- [70] Q. Fan, M. Zhang, M. Jia, S. Liu, J. Qiu, Z. Sun, Electrochemical CO2 reduction to C2+ species: heterogeneous electrocatalysts, reaction pathways, and optimization strategies, Mater. Today Energy 10 (2018) 280–301, https://doi.org/10.1016/j. mtener.2018.10.003.
- [71] G. Li, Y. Song, C. Zhu, X. Dong, W. Chen, G. Wu, G. Feng, S. Li, W. Wei, Facet-oriented Cu2O and oxygen vacancies synergistically promoting CO2 electroreduction to formate on Cu-based hollow fiber, J. CO<sub>2</sub> Util. 70 (2023) 102446, https://doi.org/10.1016/j.jcou.2023.102446.